J. Fluid Mech. (2022), vol. 935, A36, doi:10.1017/jfm.2022.35

JFM PAPERS

Acceleration statistics of tracer and light particles in compressible homogeneous isotropic turbulence

Xiangjun Wang[1,2], Minping Wan[1,3,†] and Luca Biferale[4]

[1]Guangdong Provincial Key Laboratory of Turbulence Research and Applications, Department of Mechanics and Aerospace Engineering, Southern University of Science and Technology, Nanshan District, Shenzhen, Guangdong 518055, PR China

[2]Harbin Institute of Technology, Nangang District, Harbin, Heilongjiang 150090, PR China

[3]Southern Marine Science and Engineering Guangdong Laboratory (Guangzhou), 1119 Haibin Road, Nansha District, Guangzhou, Guangdong 511458, PR China

[4]Department of Physics and INFN University of Rome 'Tor Vergata', Via della Ricerca Scientifica 1, 00133 Rome, Italy

(Received 22 May 2021; revised 24 October 2021; accepted 21 December 2021)

The accelerations of tracer and light particles (bubbles) in compressible homogeneous isotropic turbulence are investigated by using data from direct numerical simulations up to turbulent Mach number $M_t = 1$. For tracer particles, the flatness factor of acceleration components, F_a, increases gradually for $M_t \in [0.3, 1]$. On the contrary, F_a for bubbles develops a maximum around $M_t \sim 0.6$. The probability density function of longitudinal acceleration of tracers is increasingly skewed towards the negative value as M_t increases. By contrast, for light particles, the skewness factor of longitudinal acceleration, S_a, first becomes more negative with the increase of M_t, and then goes back to 0 when M_t is larger than 0.6. Similarly, differences among tracers and bubbles appear also in the zero-crossing time of acceleration correlation. It is argued that all these phenomena are intimately linked to the flow structures in the compression regions close to shocklets.

Key words: particle/fluid flow, compressible turbulence, turbulence theory

1. Introduction

Much attention has been paid to the investigation of particle-laden turbulence in recent decades. The behaviours of tracer and inertial particles in incompressible turbulence have been studied extensively, as for diffusion, collision and preferential concentration (Maxey 1987; Wang, Wexler & Zhou 1998; Zhou, Wexler & Wang 1998; Ott & Mann 2000;

† Email address for correspondence: wanmp@sustech.edu.cn

Wilkinson, Mehlig & Bezuglyy 2006; Goto & Vassilicos 2008; Coleman & Vassilicos 2009; Toschi & Bodenschatz 2009; Monchaux, Bourgoin & Cartellier 2012; Bourgoin & Xu 2014; Bragg, Ireland & Collins 2015; Gustavsson & Mehlig 2016; Wang *et al.* 2020). However, there has been much less study of compressible particle-laden turbulence, which is important for understanding flow in different domains – for example, scramjets (Ferri 1973; Curran, Heiser & Pratt 1996; Huete *et al.* 2016; Urzay 2018) and the motion of interstellar gas (Barth & Rafkin 2007; Johansen *et al.* 2007; Pan *et al.* 2011). In this paper, we will focus mainly on the acceleration statistics of tracer and light particles dispersed in compressible homogeneous and isotropic turbulence (CHIT), an idealized set-up that could be helpful to the investigation on cavitating flow with clouds of bubbles (Reisman, Wang & Brennen 1998; Wang & Brennen 1999; Fuster & Colonius 2011).

Investigation of particle acceleration in turbulence has attracted much attention in the last 20 years. Following the 'K41' theory (Kolmogorov 1941*a*,*b*), the Heisenberg–Yaglom model (Yaglom 1949; Heisenberg 1985) was proposed to predict the variance of fluid acceleration in homogeneous isotropic turbulence (HIT):

$$\langle a^2 \rangle = a_0 \varepsilon^{3/2} \nu^{-1/2}, \tag{1.1}$$

where a is the acceleration magnitude, $\langle \cdot \rangle$ represents the ensemble average, and a_0 is a universal constant, which was further found to have an anomalous dependency on the Taylor microscale Reynolds number, R_λ, owing to the turbulent intermittency (Yeung & Pope 1989; Voth, Satyanarayan & Bodenschatz 1998; Gotoh & Rogallo 1999; Vedula & Yeung 1999; Biferale *et al.* 2004). Also, $\varepsilon = 2\nu \langle S_{ij} S_{ij} \rangle$ is the average dissipation rate, S_{ij} is the rate-of-strain tensor, and ν is the kinematic viscosity. Yeung & Pope (1989) found numerically that in HIT for fluid particles, the zero-crossing time (τ_0, the time in which the autocorrelation function deceases to 0) of acceleration components is around 2.2 times the Kolmogorov time scale (τ_η). Moreover, the ratio of τ_0 to τ_η barely varies with Reynolds number, which is supported by later investigations (Yeung 1997; Voth *et al.* 1998; Mordant, Crawford & Bodenschatz 2004; Biferale & Toschi 2005; Volk *et al.* 2008*a*). Subsequently, Yeung (1997) discovered that τ_0 of the acceleration magnitude is much larger than τ_η. According to the momentum equation, the contribution to fluid acceleration can be decomposed into two parts: a pressure gradient term and a viscous force term. Vedula & Yeung (1999) pointed out that the contribution of the pressure gradient term is dominant over that of viscous force in turbulence. La Porta *et al.* (2001) confirmed experimentally that the acceleration of fluid particles is extremely intermittent in fully developed turbulence. The probability density function (p.d.f.) of acceleration components is well reproduced by a superposition of stretched exponentials (Biferale *et al.* 2004), and the flatness factor of any component, $F_a = \langle (a_i)^4 \rangle / \langle (a_i)^2 \rangle^2$, with $i = 1, 2, 3$, can exceed 60 when R_λ is up to 500. Later, many investigations on tracer particle acceleration in incompressible flows have been carried out (Voth *et al.* 2002; Mordant *et al.* 2004; Xu *et al.* 2007*a*,*b*; Lavezzo *et al.* 2010; Ni, Huang & Xia 2012; Stelzenmuller *et al.* 2017).

Apart from tracer particles, the acceleration of inertial particles (both heavy and light particles) in incompressible turbulent flows also attracted much attention. Bec *et al.* (2006) studied systematically the acceleration statistics of heavy particles in fully developed HIT. They pointed out that the flatness factor and the root-mean-square value of particle accelerations both sharply decrease with the increase of the Stokes number, $St = \tau_p / \tau_\eta$, given by the ratio of particle response time and the Kolmogorov flow time. This is a combined effect of preferential concentration on regions with small pressure gradient and filtering due to inertia. Later, Ayyalasomayajula *et al.* (2006) and Ayyalasomayajula, Warhaft & Collins (2008) proposed a vortex model to describe the selective sampling of turbulent flows and filtering effects. On the contrary, it is known that in HIT, light particles enjoy the opposite behaviour, with a strong preferential concentration on high vorticity regions, and a p.d.f. of the acceleration even more intermittent than the tracer case and – in some cases – with shorter correlation times when normalized by τ_η (Volk *et al.* 2008*a*,*b*). Recently, Zhang, Legendre & Zamansky (2019) proposed a theoretical model that predicts successfully the variance of light particles acceleration with different density ratios when *St* is small (e.g. less than 1.0), as well as the dependence of drag force and inertia force on *St*.

In recent years, developments of experimental and numerical techniques also prompted a new interest in Lagrangian properties in compressible flows (Yang *et al.* 2013, 2014, 2016; Zhang *et al.* 2016; Zhang & Xiao 2018; Dai *et al.* 2017, 2018; Xiao *et al.* 2020). Yang *et al.* (2013) investigated the accelerations of tracer particles in CHIT. They found that close to shocklets, the probability of extremely-large-acceleration events is increased. Moreover, almost all the large-acceleration events come from compression regions, and the autocorrelation function of acceleration components near shocklets decreases much faster than near vortices. Subsequently, Yang *et al.* (2014) studied the influence of shocklets on inertial particles at $M_t \approx 1.0$. They discovered that the p.d.f. of the longitudinal acceleration of light particles in compression regions has a much wider tail at the positive value than that of tracer and heavy particles. It results from the fact that light particles in compression regions have a higher probability to develop a velocity pointing upstream (the low-pressure side), compared with tracer and heavy particles. Recently, Haugen *et al.* (2022) studied the clustering of heavy particles in two different compressible isotropic flows: compressively forced turbulence and solenoidally forced turbulence. They found that the clustering of particles in compressively forced turbulence peaks at two different *St* values. The first peak (at lower *St*) results from the contribution of shocklets, and the other is attributed to the centrifugal sling effect.

In this paper, we present a systematic investigation of bubble acceleration statistics at high Reynolds numbers and changing the degree of compressibility, i.e. the turbulent Mach number, and the results will be compared with those of tracer particles. In particular, we are interested in characterizing the role played by the presence of shocklets at changing M_t concerning both the single time p.d.f. of bubble acceleration and its temporal correlation. One of the main results is the identification of a critical Mach number $M_t \sim 0.6$ where the statistics of bubbles strongly departs from that of tracers.

The outline of the paper is as follows. The numerical details are introduced in § 2. The more important results and analysis are described in § 3. Finally, a brief conclusion and discussion is given in § 4.

2. Simulation configuration

Three-dimensional CHIT was simulated in a periodic cubic box with each side of length 2π, based on a hybrid scheme (Wang *et al.* 2010) that combines the seventh-order weighted essentially non-oscillatory (WENO) scheme and eighth-order compact central finite difference scheme. The dimensionless governing equations of compressible turbulent flow are

$$\frac{\partial \rho_f}{\partial t} + \nabla \cdot (\rho_f \boldsymbol{u}) = 0, \tag{2.1}$$

$$\frac{\partial \rho_f \boldsymbol{u}}{\partial t} + \nabla \cdot (\rho_f \boldsymbol{u}\boldsymbol{u}) = -\nabla\left(\frac{p}{\gamma M^2}\right) + \frac{1}{Re}\nabla \cdot \boldsymbol{\sigma} + \boldsymbol{f}, \tag{2.2}$$

R_λ	M_t	N^3	ν	ε	η	τ_η	u_{rms}	L_f	T_f
123	0.36	512^3	4.17×10^{-3}	0.73	1.78×10^{-2}	7.59×10^{-2}	2.28	1.47	1.12
122	0.51	512^3	4.18×10^{-3}	0.78	1.75×10^{-2}	7.36×10^{-2}	2.30	1.45	1.09
122	0.64	512^3	4.20×10^{-3}	0.74	1.78×10^{-2}	7.55×10^{-2}	2.29	1.46	1.10
122	0.77	512^3	4.23×10^{-3}	0.69	1.82×10^{-2}	7.84×10^{-2}	2.27	1.48	1.13
119	0.89	512^3	4.27×10^{-3}	0.70	1.83×10^{-2}	7.84×10^{-2}	2.27	1.48	1.13
117	1.00	512^3	4.31×10^{-3}	0.63	1.89×10^{-2}	8.28×10^{-2}	2.23	1.51	1.17

Table 1. Simulation parameters: Taylor Reynolds number R_λ, turbulent Mach number M_t, grid points N^3, kinematic viscosity ν, average dissipation rate of kinetic turbulent energy ε, Kolmogorov length scale η, Kolmogorov time scale τ_η, root-mean-square fluctuation velocity $u_{rms}=\sqrt{\langle u_i u_i\rangle}$, integral length scale $L_f = \left(3\pi/(2u_{rms}^2)\right)\int_0^{+\infty}[E(k)/k]\,\mathrm{d}k$, and large-scale eddy turnover time $T_f=\sqrt{3}L_f/u_{rms}$; $E(k)$ denotes the kinetic energy at wavenumber k.

$$\frac{\partial\Theta}{\partial t}+\nabla\cdot\left[\left(\Theta+\frac{p}{\gamma M^2}\right)\boldsymbol{u}\right]=\frac{1}{\alpha}\nabla\cdot(\kappa\nabla T)+\frac{1}{Re}\nabla\cdot(\boldsymbol{\sigma}\cdot\boldsymbol{u})+\boldsymbol{f}\cdot\boldsymbol{u}+\Lambda, \tag{2.3}$$

$$p=\rho_f T, \tag{2.4}$$

where ρ_f, $\boldsymbol{u}$ and p represent the density, velocity and static pressure of fluid, respectively, and γ is the ratio of the specific heat at constant pressure, C_p, to the specific heat at constant volume, C_v. Here, $\boldsymbol{\sigma}=\mu[\nabla\boldsymbol{u}+(\nabla\boldsymbol{u})^{\mathrm{T}}]-\frac{2}{3}\mu\theta\boldsymbol{I}$ is the viscous stress, where μ is the dynamic viscosity, $\theta=\nabla\cdot\boldsymbol{u}$ is the divergence of fluid velocity, and $\boldsymbol{I}$ is the identity matrix. Also, $M=U_0/c_0$ and $Re=\rho_0 U_0 L_0/\mu_0$ are the reference Mach number and Reynolds number. Here, L_0, ρ_0, U_0, μ_0 and c_0 are the reference length, density, velocity, dynamic viscosity and speed of sound, respectively, $\Theta=p/[(\gamma-1)\gamma M^2]+\frac{1}{2}\rho_f\boldsymbol{u}\cdot\boldsymbol{u}$ is the total energy per unit volume, T denotes the temperature,and κ is the thermal conductivity; $\alpha=Pr\,Re(\gamma-1)M^2$ is a coefficient from non-dimensionalization, where Pr is the reference Prandtl number, which is specified as 0.7 in this paper. To maintain a stationary flow, an external force $\boldsymbol{f}$ is applied on the solenoidal velocity components at large scales (the first two wavenumbers). Furthermore, a uniform cooling term (Λ) is used to keep the internal energy steady. The detailed description of the forcing and cooling mechanism was introduced in Wang *et al.* (2010), Federrath *et al.* (2010) and Kida & Orszag (1990). In this paper, the turbulent Mach number (M_t) varies from 0.36 to 1.00, with Taylor Reynolds number $R_\lambda\approx120$, and the total grid number (N^3) in the computational domain is 512^3. Detailed parameters of the simulations are listed in table 1.

The light particles are regarded as point objects, neglecting the influence of particles on turbulent flows and their mutual interaction. The motion of light particles is governed by

$$\frac{\mathrm{d}\boldsymbol{x}_p}{\mathrm{d}t}=\boldsymbol{v}_p, \tag{2.5}$$

$$\frac{\mathrm{d}\boldsymbol{v}_p}{\mathrm{d}t}=\frac{\boldsymbol{u}_p-\boldsymbol{v}_p}{\tau_p}+\beta\frac{\mathrm{D}\boldsymbol{u}_p}{\mathrm{D}t}, \tag{2.6}$$

$$\tau_p=\frac{\rho_f d^2}{12\beta\mu}, \tag{2.7}$$

$$\beta=\frac{3\rho_f}{2\rho_p+\rho_f}, \tag{2.8}$$

M_t	0.36	0.51	0.57	0.64	0.77	0.89	1.00
$a_{rms}(Tracer)$	8.41	9.02	9.19	9.68	10.82	11.63	11.75
$a_{rms}(Light)$	9.74	11.74	13.87	17.82	28.86	45.27	52.95

Table 2. Values for a_{rms} of tracers and bubbles at different M_t values.

where $\boldsymbol{x}_p$, $\boldsymbol{v}_p$, τ_p and d are the position, velocity, response time and diameter of particles, respectively, and $\boldsymbol{u}_p$ is the velocity of the flow at the position of the particle. Here, μ is the dynamic viscosity of fluid at the position of particles, and we notice that both τ and β are dependent on space and time due to the variation of the underlying fluid density ρ_f. As a result, in a compressible flow, even a particle with density ρ_p equal to the average flow density $\langle\rho_f\rangle$ will nevertheless be locally subjected to inertial forces due to the variation of the local flow density, where $\beta = 1$ denotes the transition from particles heavier to lighter than the surrounding flow. In our case we have chosen $\rho_p = 0.01\langle\rho_f\rangle$ for the light particles. It is important to stress that (2.6) must be considered an approximation of the true point-like description of inertial forces. Besides corrections present also in incompressible forces, as the Faxen and Basset terms (Maxey & Riley 1983; Gatignol 1983), here we also need to consider new forces induced by density variations of the fluid flow at the particle positions (Parmar, Haselbacher & Balachandar 2011, 2012). In Appendix A we present a thoughtful discussion about these new effects and show that at moderate Mach numbers, such as the one investigated here, they can be safely neglected most of the time. The fluid velocity at the position of particles, $\boldsymbol{u}_p$, is evaluated by a fourth-order Lagrangian interpolation. The operator $\mathrm{D}/\mathrm{D}t$ represents the material derivative. The number of particles that are uniformly released into the computational domain after the flow reaches a statistically steady state is 256^3. After the particles are fully mixed, we sample over 15 times large-eddy turnover time (T_f) to explore the spatial, instantaneous statistics of particles. The Stokes number ($St = \tau_p/\tau_\eta$) of particles is approximately 0.21, and the average of β is around 2.94. In addition, tracer particles whose velocity follows the local fluid velocity are analysed for comparison.

3. Results and analysis

Before presenting the results from the statistical analysis, we show in figure 1 some characteristic evolution of the acceleration magnitudes, a, along tracers and light particles trajectories near strong compression structures (e.g. shocklets) at $M_t = 0.51$ and $M_t = 1.00$, colour coded in terms of the local fluid compressibility θ. For tracer particles, there is no significant difference between $M_t = 0.51$ and 1.00, except for the larger peak of acceleration magnitudes near shocklets at $M_t = 1.00$. For bubbles at $M_t = 0.51$, the evolution of acceleration magnitudes is similar to that of tracer particles. However, at $M_t = 1.00$, bubbles seem to be trapped near the shocklets for a long time (several times τ_η), and the acceleration magnitudes of particles fluctuate dramatically. For the sake of completeness, the root-mean-square of acceleration magnitudes, a_{rms}, is shown in table 2. As one can see, as M_t increases from 0.36 to 1.00, a_{rms} of tracers increases slightly, whereas a_{rms} of bubbles increases dramatically with increasing M_t, especially for $M_t > 0.64$. In addition, for light particles the root-mean-square values of the two terms in the right-hand side of (2.6) are also measured (not shown). The root-mean-square of the drag term is comparable to (slightly smaller than) that of the $\beta\, \mathrm{D}\boldsymbol{u}_p/\mathrm{D}t$ term at all M_t.

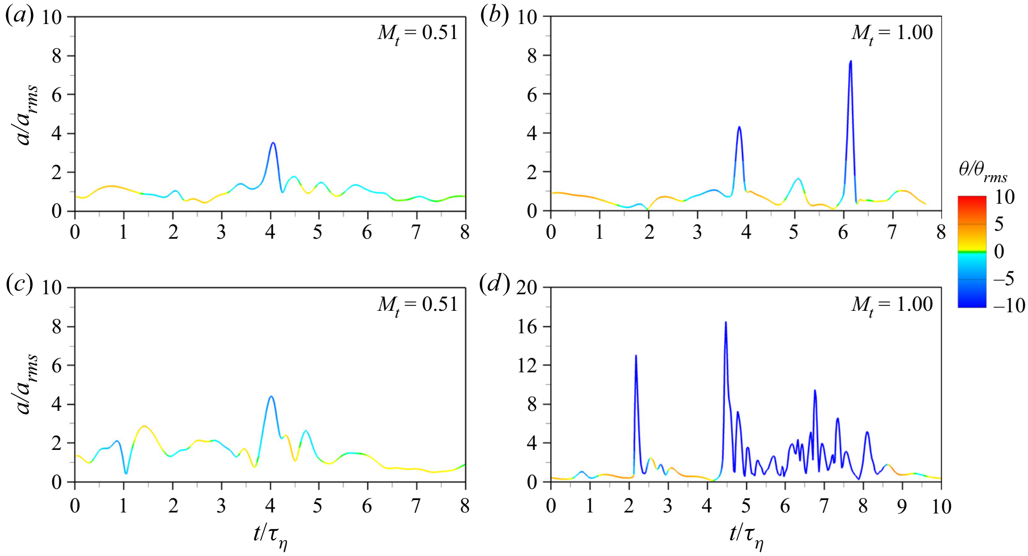

Figure 1. The evolution of the acceleration magnitude, a, of typical tracers (a,b) and light particles (c,d) at $M_t = 0.51$ and $M_t = 1.00$. The colourbar indicates the divergence of fluid velocity, θ, at the position of particles. Here a_{rms} and θ_{rms} represent the root- mean-square values of a and θ, respectively.

The p.d.f.s of one component of the particle accelerations, a_i, with $i = 1, 2, 3$, are illustrated in figure 2. It is apparent that all p.d.f.s have some intense stretched tails, indicating that the accelerations of tracer and bubbles are both intermittent. Unfortunately, the multifractal model used to predict successfully the p.d.f. of acceleration for tracers (Biferale *et al.* 2004) in incompressible flows cannot be translated easily to the case of inertial particles. This is due to the fact that it is not known how to correlate the local fluctuations of the Kolmogorov time with the effects of preferential concentration and filtering induced by the presence of inertia. Furthermore, the compressible effects add another direction that is not fully under control with the multifractal approach. The strength of intermittency can be quantified by the flatness of the acceleration component defined as $F_a = \langle (a_1)^4 \rangle / \langle (a_1)^2 \rangle^2$, where here by $\langle \cdot \rangle$ we indicate the average among all particles. For tracers, F_a increases steadily with the increase of M_t, as seen in figure 3. However, F_a of light particles does not follow this trend. As M_t increases from 0.36 to 1.00, F_a of bubbles first increases, then reduces after M_t exceeds about 0.6. The increase of F_a of tracer particles (also applicable for bubbles at $M_t < 0.6$) is attributed to the fact that increasing compressibility increases the flow intermittency. However, when $M_t > 0.6$, why does F_a of light particles decrease with the increase of M_t? Figure 4 shows the marginal cumulated distribution $P(a, \theta_m) = \int_{-\infty}^{\theta_m} P(a, \theta)\, \mathrm{d}\theta$ of particle acceleration components conditioned to fall in different flow regions. We define CR1, CR2 and CR3 to represent the flow regions where $\theta_m < -\theta_{rms}$, $\theta_m < -2\theta_{rms}$ and $\theta_m < -3\theta_{rms}$ separately. For the sake of clarity, we mark the boundaries of CR1, CR2 and CR3 in figure 5 where the p.d.f.s of the divergence of fluid velocity at different M_t are shown. Figure 4 reflects that the stretched tails of acceleration p.d.f.s result predominantly from the particles in strong compression regions when $M_t > 0.6$. In addition, F_a is impacted heavily by the tails of acceleration p.d.f.s, as shown in the insets of figure 2. Therefore, we argue that the decrease of F_a should be related to the statistical properties of bubbles in compression regions when $M_t > 0.6$.

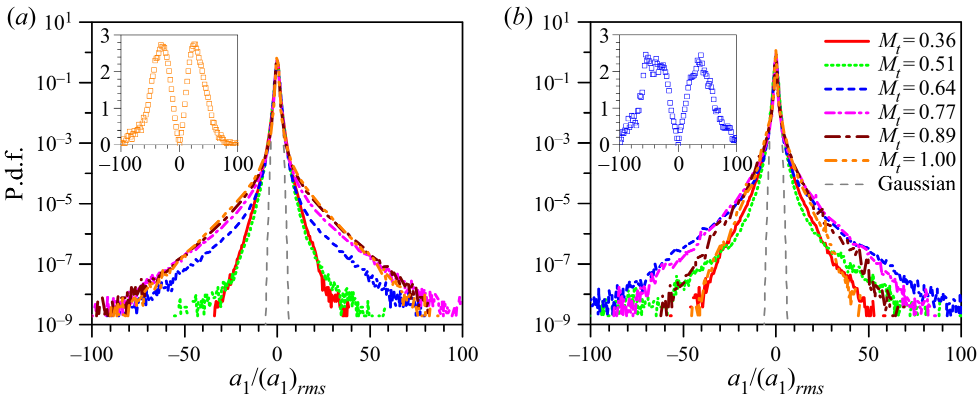

Figure 2. The p.d.f.s, $P(a_i)$, of one component of the accelerations a_i, normalized with its root-mean-square. Because of isotropy, all three components are equivalent. For clarity, here we show only the case with $i = 1$. Panel (*a*) is for tracer particles. Inset: $(a_1)^4P(a_1)$ at $M_t = 1.00$ is presented to check the statistical convergence of the fourth-order moments. Panel (*b*) is for light particles. Inset: $(a_1)^4P(a_1)$ is shown at $M_t = 0.64$.

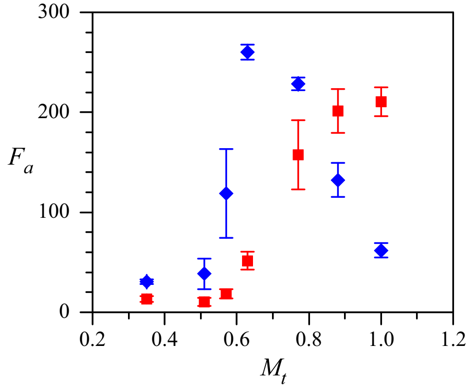

Figure 3. The flatness factor of particle acceleration components, F_a, at changing M_t for tracers (red squares) and light particles (blue diamonds). The error bar is calculated from the scatter among 30 subsamples obtained from 30 time snapshots.

Let us first compare F_a values of light particles in different regions, as shown in figure 6, where: case 1 represents the whole domain; case 2 represents the region with $\theta > -3\theta_{rms}$ (removing CR3 from case 1); case 3 represents the region with $\theta > -2\theta_{rms}$ (removing CR2 from case 1); case 4 represents the region with $\theta > -\theta_{rms}$ (removing CR1 from case 1). We can notice that at $M_t = 0.64$, F_a decreases sharply once the light particles in CR3 are removed. In contrast, at $M_t = 1.00$, F_a increases steadily as the particles in CR3, CR2 and CR1 are removed. Figure 7 also shows the p.d.f.s of a_1 of light particles at cases 1, 2, 3 and 4 when $M_t = 0.64$ and 1.00. The tails of the p.d.f.s of a_1 for $M_t = 0.64$ become much narrower when the light particles in strong compression regions are removed, whereas the tails, at $M_t = 1.00$, become wider since the light particles in CR3, CR2 and CR1 are removed. To explain this difference, in figure 8, we compare the number of bubbles and tracers in CR3. Here, we can see that the number of tracers keeps a quite low level when $M_t \in [0.36, 1.00]$ although it is slightly increasing. On the other hand, the number of bubbles in CR3 increases dramatically when $M_t > 0.6$,

https://doi.org/10.1017/jfm.2022.35 Published online by Cambridge University Press

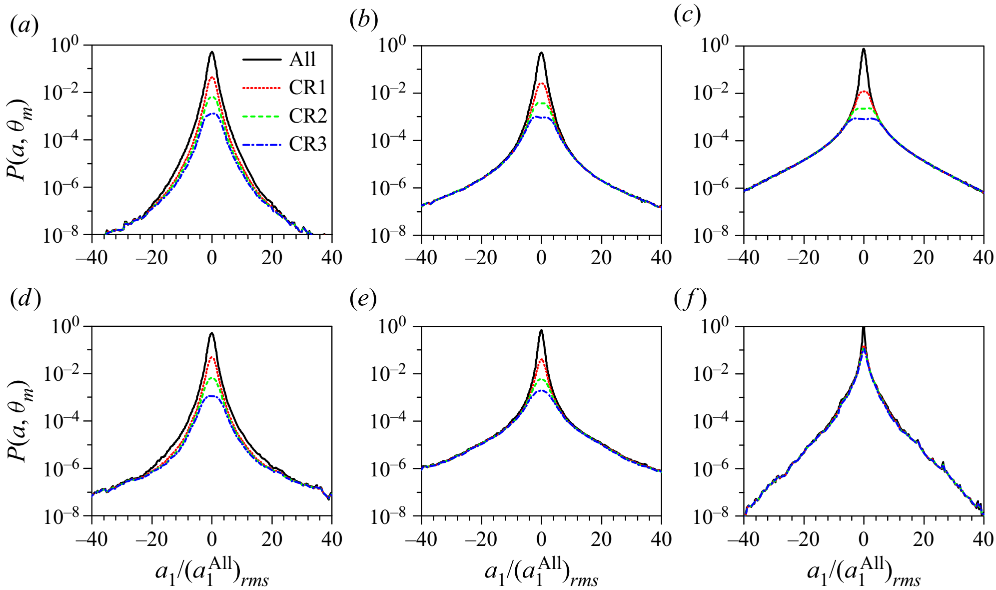

Figure 4. The cumulated marginal p.d.f.s of particle acceleration components $P(a, \theta_m)$, with $\theta_m = -\theta_{rms}$, $-2\theta_{rms}$ and $-3\theta_{rms}$ for CR1, CR2 and CR3, respectively. The black solid line is the reference p.d.f. obtained by considering the particles on the whole computational domain ($\theta_m = +\infty$). The red dotted, green dashed and blue dash-dotted lines are for CR1, CR2 and CR3, respectively. Panels (*a–c*) are for tracer particles at $M_t = 0.51$, 0.64 and 1.00, respectively; (*d–f*) are for light particles at $M_t = 0.51$, 0.64 and 1.00.

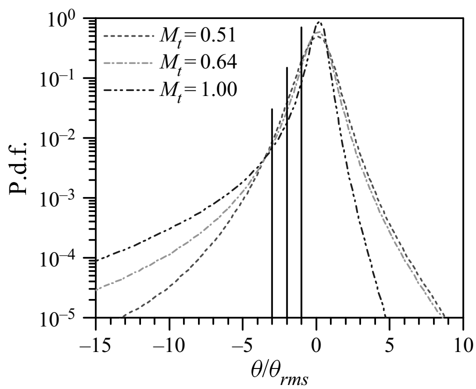

Figure 5. The p.d.f.s of the divergence of fluid velocity, θ, evaluated in the whole computational domain at $M_t = 0.51, 0.64$ and 1.00. The three vertical lines separately mark the boundaries of CR1, CR2 and CR3, where $\theta < -\theta_{rms}$, $\theta < -2\theta_{rms}$ and $\theta < -3\theta_{rms}$.

especially at $M_t = 1.00$, accounting for approximately 25 % of the total particle number in the whole domain. That is, bubbles will accumulate significantly in strong compression regions (near shocklets). Figure 9 shows the distribution of light particles and θ in a quasi-two-dimensional slice with $M_t = 0.64$ and 1.00. As one can see, bubbles tend to accumulate in strong compression regions at $M_t = 1.00$, which is different to what happens at $M_t = 0.64$. In order to understand the preferential concentration, it is key to control the divergence of particles' velocities as derived from (2.6), and assuming that β and τ_p do

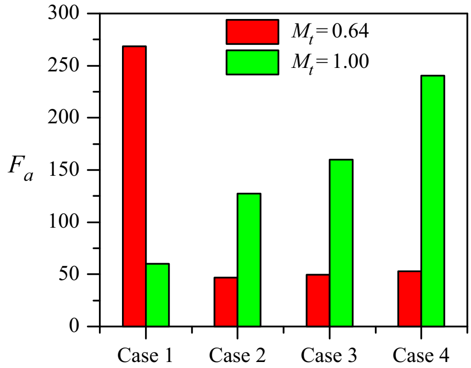

Figure 6. F_a of light particles in different regions: case 1, the whole domain; case 2, the regions with $\theta > -3\theta_{rms}$ (removing CR3 from case 1); case 3, the regions with $\theta > -2\theta_{rms}$ (removing CR2 from case 1); case 4, the regions with $\theta > -\theta_{rms}$ (removing CR1 from case 1).

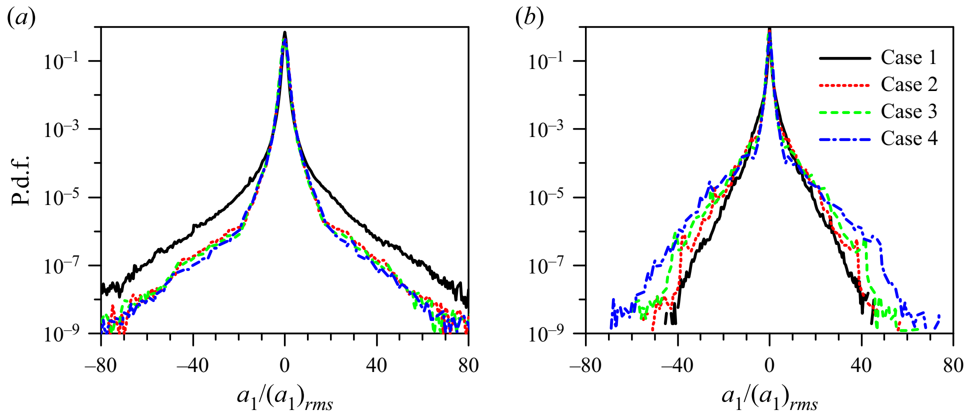

Figure 7. The p.d.f.s of a_1 of light particles in different regions when $M_t = 0.64$ (*a*) and $M_t = 1.00$ (*b*).

not vary significantly with space and time, we have

$$\nabla \cdot \boldsymbol{v}_p \approx \theta + \tau_p(1-\beta)\left(Q - \frac{\mathrm{D}\theta}{\mathrm{D}t}\right). \tag{3.1}$$

Here, $Q = \Omega_{ij}\Omega_{ij} - S_{ij}S_{ij}$ is the second-order invariant of fluid velocity gradients, where Ω_{ij} and S_{ij} are the rate-of-rotation tensor and rate-of-strain tensor, respectively, and $\mathrm{D}\theta/\mathrm{D}t = \partial\theta/\partial t + \boldsymbol{u}\cdot\nabla\theta$ is the material derivative of θ. From (3.1) one can see that light particles ($\beta > 1$) tend to accumulate in the regions $\theta < 0$, $Q > 0$ and $\mathrm{D}\theta/\mathrm{D}t < 0$. From the above expression, it is clear that the prediction on preferential concentration for the case of inertial particles in compressible flows is much more complicated than in the incompressible case, being connected to cross-correlations among compressibility of the carrying flow, inertia parameters and local flow topology. In order to achieve a systematic understanding of such a complex phenomenon, one would need refined scanning at changing of τ_p and β parameters too, which is outside the scope of this paper.

According to figure 4, one can understand that the particles with extremely large accelerations come predominantly from the strong compression regions (such as CR3) at high M_t. Then, if the number of particles in CR3 is small (like tracers), the probability

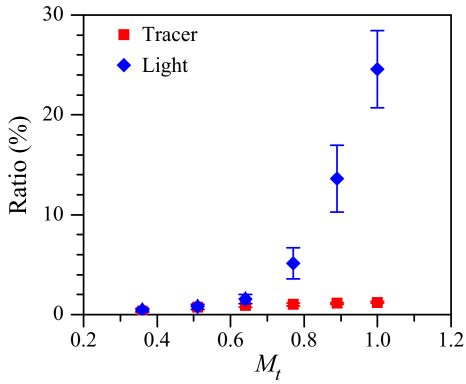

Figure 8. The ratio of the particle number in CR3 to the total particle number in the whole domain.

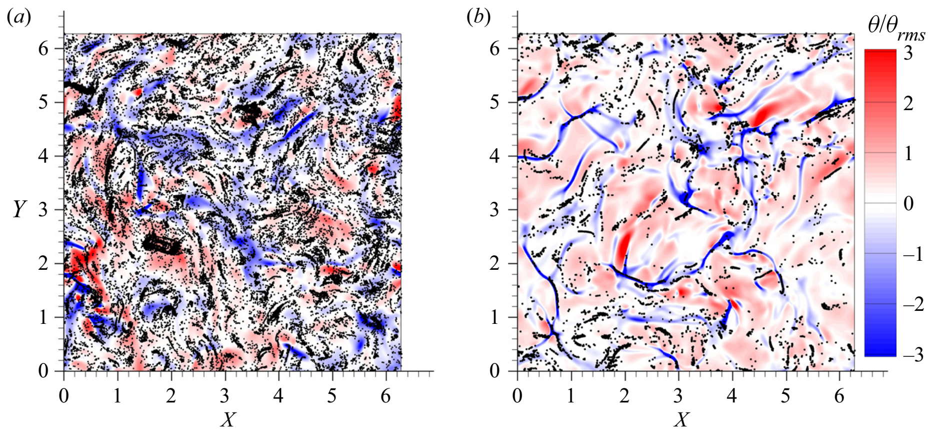

Figure 9. The distribution of light particles and θ in a two-dimensional slice when $M_t = 0.64$ (*a*) and $M_t = 1.00$ (*b*). Here, all particles lie in a quasi-two-dimensional slice with a width in the third dimension of the order of the Kolmogorov length scale. X and Y represent the x-coordinate and y-coordinate of slices.

of the particles with large accelerations is still small. Therefore, a slight increase of particle number in CR3 will make a contribution to the enhancement of the acceleration intermittency. Hence F_a of tracers increases with the increase of M_t. On the other hand, if the number of particles in CR3 is large, as for the case of bubbles at $M_t = 0.77$–1.00, there will be a large portion of particles with large accelerations, which can no longer be regarded as rare events. Then the increase of particle number in CR3 will no longer contribute to the increase of acceleration intermittency. As a result, the preferential concentration of bubbles in strong compression regions (e.g. CR3) results in the decrease of F_a when $M_t > 0.6$. In order to further validate this mechanism, the flatness factor of acceleration components of fluid elements at the position of bubbles, F_a^u, is measured, shown in figure 10 where F_a^u varies with the same trend as F_a of light particles. Therefore, we confirm that the decrease of F_a of light particles at $M_t > 0.6$ is attributed to the preferential concentration of light particles in strong compression regions.

It is also worth explaining why F_a of light particles increases dramatically at $M_t \in [0.5, 0.6]$. One understands that the particles in CR3 (near shocklets) have large accelerations in general. Figure 8 shows that the number of tracers in CR3 always keeps a

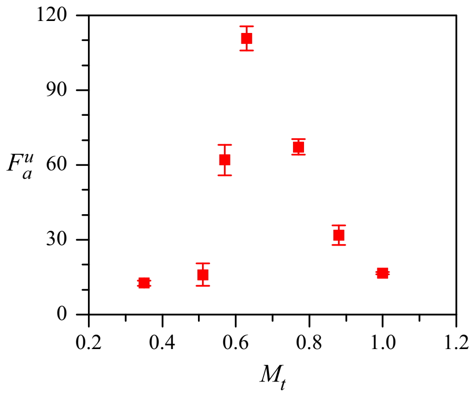

Figure 10. The flatness factor of acceleration components of fluid elements at the position of light particles, F_a^u, versus M_t.

quite low level, and it slightly increases as M_t increases from 0.36 to 1.00, resulting in a significant increase of the intermittency of acceleration. Therefore, F_a of tracers increases steadily with increasing M_t. The number of bubbles is also low when $M_t < 0.6$, but it increases faster than the number of tracers at $M_t \in [0.5, 0.6]$, so that the number of light particles in CR3 at $M_t = 0.64$ has been up to that of tracers at $M_t = 1.00$, leading to a fast increase of F_a.

3.1. *Longitudinal acceleration at different M_t*

The longitudinal acceleration, $a_L = (\boldsymbol{a} \cdot \boldsymbol{v}_p)/|\boldsymbol{v}_p|$, is the projection of acceleration ($\boldsymbol{a}$) to the direction of particle velocity ($\boldsymbol{v}_p$), which determines how fast the magnitude of velocity varies. Figure 11 presents the p.d.f.s of a_L of particles at $M_t = 0.36$–1.00. One can see that for tracers, the p.d.f.s of $\boldsymbol{a}_L$ are skewed towards negative values. However, for bubbles, the p.d.f.s of $\boldsymbol{a}_L$ skew only moderately to the negative value at low M_t (e.g. $M_t = 0.51$), and this trend vanishes as the p.d.f.s become almost symmetric at high M_t (e.g. $M_t = 1.00$). To quantify this difference, we measure the skewness factor of $\boldsymbol{a}_L$, S_a, as shown in figure 12. For tracers, S_a becomes more negative as M_t increases from 0.36 to 1.0. As is well known, shocklets will appear in compression regions with the increase of M_t. When tracer particles pass through the shocklets from upstream to downstream, they will be decelerated significantly owing to the negative pressure gradient (Anderson 2010). As M_t increases, the shocklets become stronger (the deceleration is also more remarkable). Therefore, the p.d.f. of $\boldsymbol{a}_L$ is more skewed to negative values and S_a becomes more negative for tracers when M_t increases.

As shown in figure 12, for light particles, S_a also decreases with M_t when M_t is small, similar to the situation for tracers. However, S_a gradually goes back to zero after $M_t > 0.6$. A similar phenomenon was suggested by Yang *et al.* (2014), who discovered that S_a of light particles in compression regions is close to 0 at $M_t \approx 1.03$, and there are many light particles whose velocities have an obtuse angle with local pressure gradient. To understand the above difference between tracers and bubbles, we show in figure 13 the p.d.f. of $\cos\alpha$ in CR1 (compression region with $\theta < -\theta_{rms}$), where α is the angle between the velocity of particles and the local pressure gradient. One can see that most tracers in CR1 have angle $\alpha < 90^\circ$ ($\cos\alpha > 0$) at all M_t. However, for light particles, the number of particles with $\alpha > 90^\circ$ ($\cos\alpha < 0$) increases steadily as M_t increases from 0.6 to 1.0 approximately.

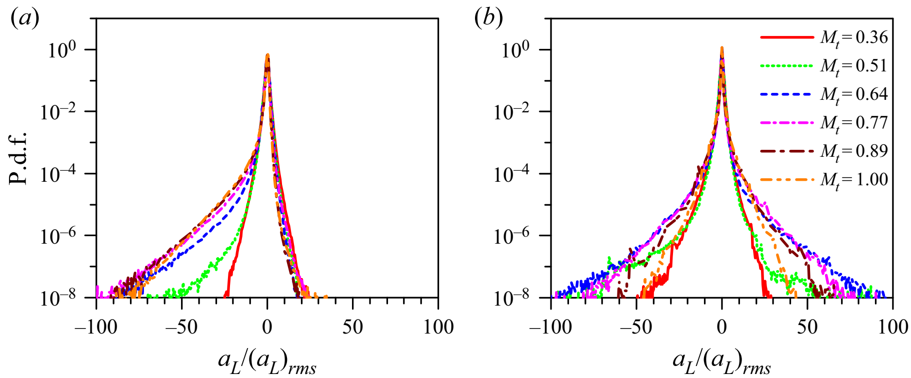

Figure 11. The p.d.f.s of longitudinal accelerations for (*a*) tracer particles, (*b*) light particles.

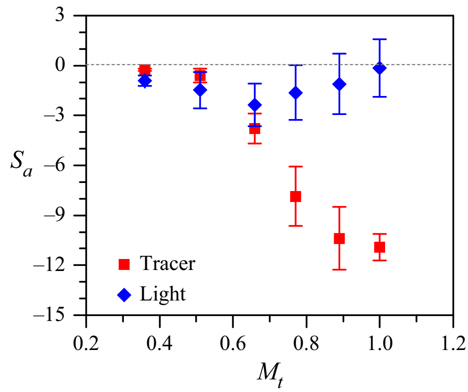

Figure 12. The skewness factor of particle longitudinal accelerations, S_a, varies with M_t.

Then we measure how many particles have angle $\alpha < 90^\circ$ before entering CR1, denoted as N_{CR1}^{in}, and once inside CR1, denoted as N_{CR1}. Figure 14 shows that for tracer particles, N_{CR1} is always close to N_{CR1}^{in} at different M_t. That is, tracers rarely change their direction in CR1. However, for light particles, N_{CR1} is noticeably smaller than N_{CR1}^{in} at high M_t, and this deviation becomes more significant as M_t increases. That is, as M_t increases, more bubbles reverse their direction of velocity from $\alpha < 90^\circ$ to $\alpha > 90^\circ$ in CR1, so that more light particles that were decelerated turn to be accelerated. This is the main reason for the p.d.f. of $\boldsymbol{a}_L$ being more symmetric when $M_t > 0.6$. Also, N_{CR1} of light particles decreases moderately as M_t increases from 0.6 to 1.0, which implies that at high M_t, more light particles have positive longitudinal accelerations when they are entering CR1.

Why do many light particles reverse their velocity direction from $\alpha < 90^\circ$ to $\alpha > 90^\circ$ in CR1, but few tracers do? As one can see from (2.6), the effect of local fluid acceleration on light particles is amplified by β ($\beta \approx 2.94$ in our simulations). Thus it is easier to decelerate light particles by the negative pressure gradient near shocklets, compared with tracers. Assuming that a tracer and a light particle enter the shocklets from upstream at the same time, both will be decelerated under the negative pressure gradient. In general, the tracer particle can pass through the shocklets successfully. However, the velocity of the light particle could decrease to zero, or even have its direction reversed since β amplifies

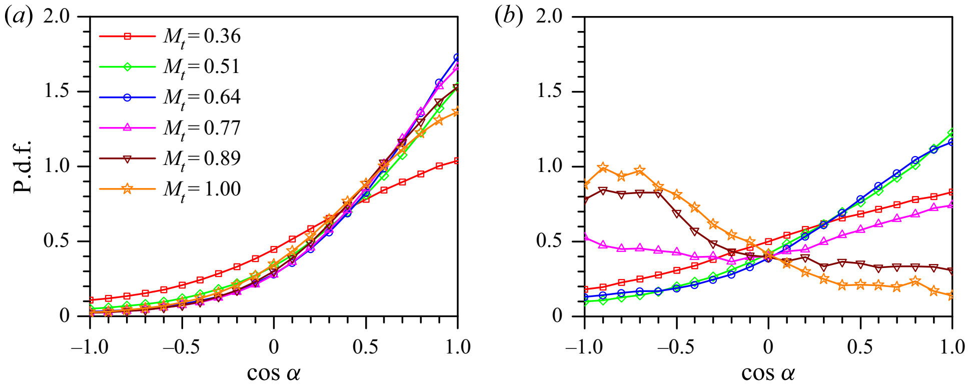

Figure 13. The p.d.f.s of $\cos\alpha$ in CR1. Here, α is the angle between the velocity of particles and the local pressure gradient: (*a*) tracer particles; (*b*) light particles.

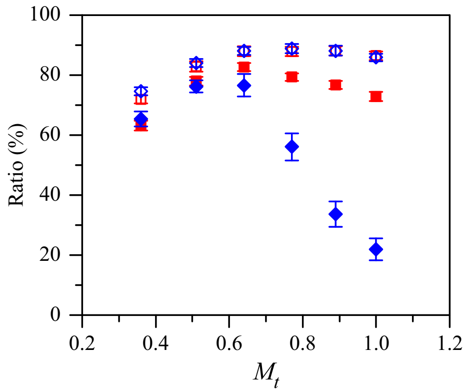

Figure 14. The ratios of N^{in}_{CR1} (red squares) and N_{CR1} (blue diamonds) to the total number of particles in CR1. The empty symbols are for tracers, and the filled symbols are for light particles. Here, N^{in}_{CR1} denotes the number of particles with $\alpha < 90^\circ$ when entering CR1, and N_{CR1} denotes the number of particles with an angle of $\alpha < 90^\circ$ in CR1.

the effect of negative pressure gradient. For example, the comparison between N^{in}_{CR1} and N_{CR1} in figure 14 reflects quantitatively that at $M_t = 1.00$, 51 % of light particles in CR1 reverse their velocity direction from $\alpha < 90^\circ$ to $\alpha > 90^\circ$, but few tracer particles do.

3.2. *Autocorrelation function of acceleration components at different M_t*

Figure 15 shows the autocorrelation function of the first component of accelerations $R_1(\tau) = \langle a_1(t)\, a_1(t+\tau)\rangle / \langle a_1(t)^2\rangle$ (because of isotropy, R_2 and R_3 would be equal to R_1). One can notice that in the small time scale, the R_1 values for tracers and bubbles both decrease faster for increasing M_t. However, for tracers, the zero-crossing time, τ_0, barely varies with M_t, and it is approximately close to $2.3\tau_\eta$, which is similar to the results in incompressible turbulence (Yeung 1997; Mordant *et al.* 2004; Volk *et al.* 2008*a*). For bubbles, τ_0 is also approximately equal to $2.3\tau_\eta$ when $M_t < 0.6$. In fact, it is slightly smaller than the value for tracer particles, as shown in figure 16. Volk *et al.* (2008*a*) found that τ_0 of light particles in incompressible homogeneous isotropic turbulence is

https://doi.org/10.1017/jfm.2022.35 Published online by Cambridge University Press

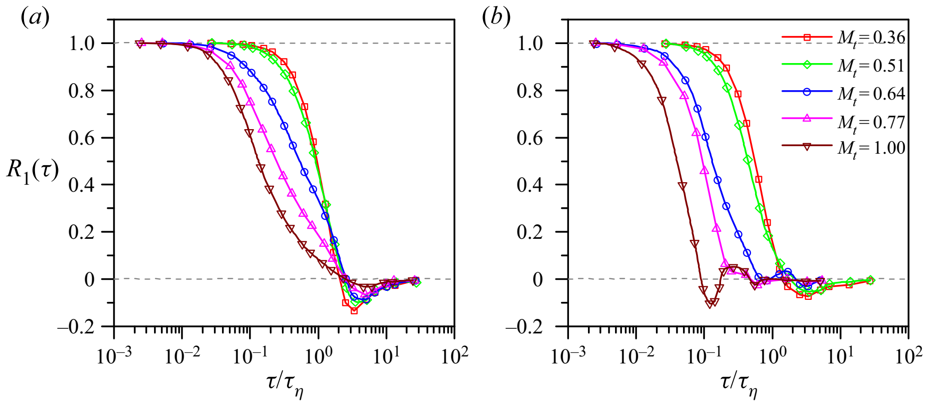

Figure 15. The autocorrelation function, $R_1(\tau)$, of a_1 at different M_t, for (*a*) tracers, (*b*) light particles.

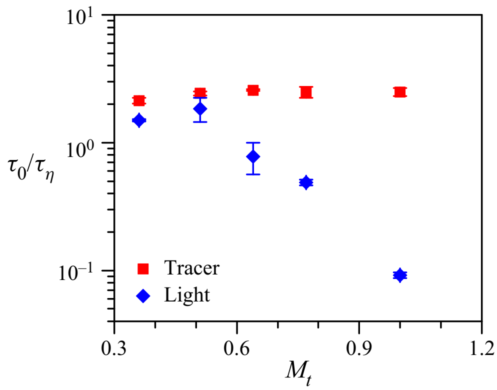

Figure 16. τ_0 varies with M_t for tracers (red squares) and light particles (blue diamonds).

significantly smaller than the value for tracers, which is slightly different from our results. This might be attributed to the fact that $St = 1.64$ in the work by Volk *et al.* (2008*a*), whereas $St \approx 0.2$ in our simulations. Also shown in figure 16 is that when $M_t > 0.6$, τ_0 of light particles will gradually decrease with the increase of M_t, unlike the value for tracer particles.

Why is the trend of the changes of τ_0 between tracer and light particles different from each other at high M_t? Yang *et al.* (2013) found that the autocorrelation function of acceleration of tracers near shocklets decreases much faster than that near vortices in CHIT. In addition, we use the persistence time τ_c to denote the period needed for the particles to pass across the strong compression regions (CR3), as shown in figure 17(*a*). It is found that the average of τ_c among tracers, $\langle \tau_c \rangle$, is smaller than τ_η, and it decreases slightly with the increase of M_t ($\langle \tau_c \rangle \approx 0.2\tau_\eta$ at $M_t = 1.00$), as shown in figure 17(b). For light particles, $\langle \tau_c \rangle$ is similar to that for tracer particles when $M_t < 0.6$. However, as M_t increases further, $\langle \tau_c \rangle$ increases dramatically, up to around $4\tau_\eta$ at high M_t. Then one can argue that $R_1(\tau)$ of tracers is barely influenced by shocklets since the time that tracers stay in strong compression regions is quite short. Therefore, $\tau_0 \approx 2.34\tau_\eta$ of tracers is independent of M_t and close to the value of the small-scale eddy turnover time. For light particles, at low M_t (e.g. $M_t = 0.51$), $\langle \tau_c \rangle$ is similar to that for tracers so that τ_0 of

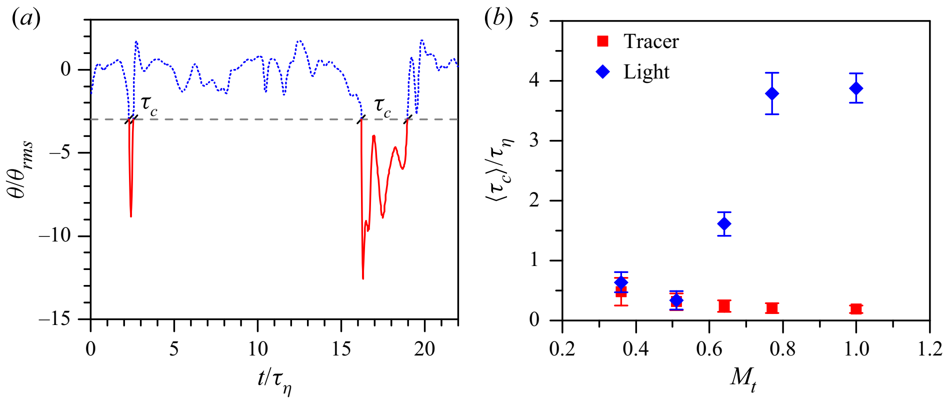

Figure 17. (a) The history curve of θ along one trajectory of bubble at $M_t = 1.00$. Here, τ_c denotes the time over which particles pass through CR3. (b) The average value of characteristic time of particles staying in CR3, $\langle \tau_c \rangle$, at different M_t.

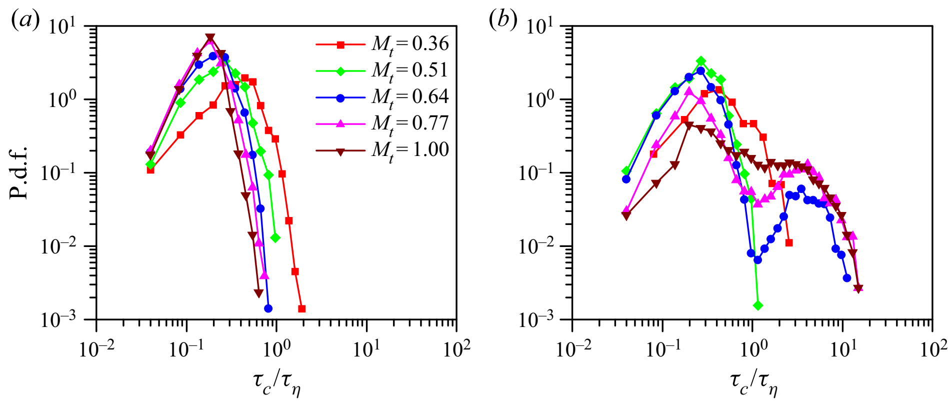

Figure 18. The p.d.f.s of the time (τ_c) that particles stay in strong compression regions (CR3) at different M_t, for (a) tracers, (b) light particles.

bubbles is quite close to that of tracers. However, as M_t increases, $\langle \tau_c \rangle$ of light particles increases gradually because more bubbles will be trapped in strong compression regions (near shocklets) for several τ_η, as shown in figure 18(b), where the p.d.f.s of τ_c of light particles present two peaks when $M_t > 0.6$, which is different to what happens for tracers; see figure 18(a). The position of the first peak ($\tau_c/\tau_\eta = 0.2$–0.3) is similar to that of tracers. However, the second peak occurs in the range of $\tau_c/\tau_\eta = 3.0$–4.0, indicating that many bubbles are trapped by shocklets, hence the influence on $R_1(\tau)$ becomes remarkable, and τ_0 of light particles decreases with increasing M_t. In order to confirm the above conclusion further, we have measured $R_1(\tau)$ for light particles when the events of $\tau_c > 1.0$ are removed at $M_t = 1.00$, as shown in figure 19. As expected, $R_1(\tau)$ for light particles decreases much more slowly when the events of $\tau_c > 1.0$ are removed, and τ_0 increases by approximately five times. Therefore, we confirm the observation that the decrease of τ_0 with increasing M_t is attributed to the larger number of light particles that are trapped near shocklets for a long time.

It is also worth noting the oscillation of $R_1(\tau)$ for light particles at high M_t, as shown in figure 15(b). From the preceding analysis, bubbles could be trapped in vortices and near

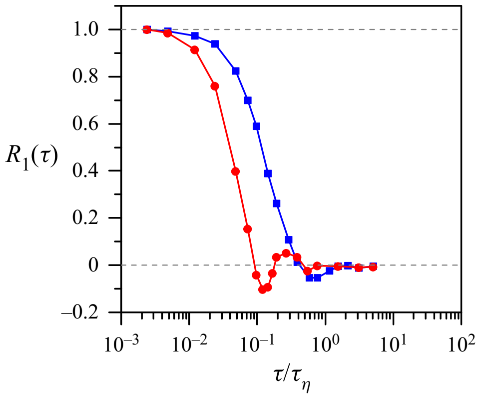

Figure 19. For light particles, $R_1(\tau)$ at $M_t = 1.00$ after the events of $\tau_c > 1.0$ are removed (blue squares) compared with the unconditioned case (red circles).

shocklets for comparable time scales. We believe that the strong oscillatory behaviour is the combined effect of both vortices and shocklets, as confirmed by plotting the conditioned autocorrelation function in figure 19, where the oscillation disappears when the events of $\tau_c > 1.0$ have been removed.

4. Conclusion and discussion

The acceleration statistics of tracer and light particles (bubbles) in CHIT have been studied. Our main finding is related to the characteristic signature of the presence of shocklets in the probability density function of acceleration and on its characteristic correlation times. In particular, we found that at $M_t \sim 0.6$, the statistical properties of bubble acceleration start to be strongly different from those of the underlying tracers, developing a sort of *condensation* on and near shocklet structures, where a high percentage of the total number of particles is concentrated. As a consequence, acceleration flatness, skewness and autocorrelation time are strongly affected. We find that in the range investigated here, $M_t \in [0.31, 1]$ the flatness factor of acceleration components, F_a, of tracers increases monotonically with M_t. For light particles, F_a also increases with M_t at $M_t < 0.6$. However, when $M_t > 0.6$, F_a of bubbles decreases with M_t because of preferential accumulation in strong compression regions.

The p.d.f.s of the longitudinal acceleration of tracers are found to be skewed towards negative values, and as M_t increases, the skewness factor, S_a, becomes more negative. For light particles, S_a also becomes more negative with the increase of M_t, followed by a tendency to return to 0 after $M_t > 0.6$. We attribute the tendency of the longitudinal acceleration p.d.f. of light particles to become more and more symmetric at high M_t to the fact that more particles reverse their direction of velocity from $\alpha < 90^\circ$ to $\alpha > 90^\circ$ in compression regions (e.g. regions with $\theta < -\theta_{rms}$) at increasing compressibility, together with the fact that more bubbles with positive longitudinal acceleration enter compression regions at higher M_t.

We have found that for tracers, the characteristic persistence time, τ_c, near shocklets is quite short, especially at high M_t ($\langle \tau_c \rangle \approx 0.2\tau_\eta$ at $M_t = 1.00$). Hence the autocorrelation function of acceleration components, $R_1(\tau)$, decreases faster at higher M_t in the small time scale, while the zero-crossing time, τ_0, does not vary too much with M_t. For light particles, as M_t increases, larger number of particles are trapped near shocklets for several

τ_η, so the influence of shocklets on the autocorrelation function of accelerations becomes remarkable. Therefore, τ_0 is influenced greatly by shocklets and decreases with M_t.

The results in this paper are obtained under the point-particle approximation, supposing that the radius of tracers and bubbles is not larger than the Kolmogorov length scale (η). Furthermore, it is important to make sure also that the typical width of shocklets is not too small, in order to not break the validity of the above assumption. In our direct numerical simulations, even the stronger shocklets have a size within $2\eta \sim 3\eta$, keeping the approximation reasonably valid.

The strong singular signature of shocklets for the dynamics and statistics of light particles opens up many important questions that need further numerical and experimental studies. In particular, the role of correction terms in (2.6) induced by the presence of compressibility must be better elucidated, as discussed in Appendix A. Second, in the presence of strong particles' concentration near shocklets, the importance of bubble–bubble collision, breakup and coalescence should be quantified better, as well as their feedback on the flow. Finally, future work also needs to provide detailed studies of preferential concentration properties when changing both the Stokes time and added mass parameters, in order to have more comprehensive control of the behaviour of inertial particles at changing Mach number.

Funding. We are grateful to Professor J. Wang for providing the DNS code for CHIT. This work is funded by the National Numerical Wind Tunnel Project (no. NNW2019ZT1-A01), the National Natural Science Foundation of China (grant no. 91752201), the Department of Science and Technology of Guangdong Province (grant no. 2019B21203001), the Key Special Project for Introduced Talents Team of Southern Marine Science and Engineering Guangdong Laboratory (Guangzhou) (grant no. GML2019ZD0103), and the Shenzhen Science and Technology Innovation Committee (grant no. KQTD20180411143441009). We acknowledge computing support provided by the Center for Computational Science and Engineering of the Southern University of Science and Technology. L.B. acknowledges hospitality from the Southern University of Science and Technology and funding from the European Research Council (ERC) under the European Unions Horizon 2020 research and innovation programme (grant agreement no. 882340).

Declaration of interests. The authors report no conflict of interest.

Author ORCIDs.
Minping Wan https://orcid.org/0000-0001-5891-9579;
Luca Biferale https://orcid.org/0000-0001-8767-9092.

Appendix A

According to Parmar *et al.* (2012), the governing equation for the movement of light particles in compressible turbulence can be expressed (neglecting history force) as

$$\rho_p \frac{\mathrm{d}\boldsymbol{v}_p}{\mathrm{d}t} = \frac{9\mu}{2a^2}\left(\boldsymbol{u}_p - \boldsymbol{v}_p\right) + \rho_f \frac{\mathrm{D}\boldsymbol{u}_p}{\mathrm{D}t} + \frac{1}{2}\left[\frac{\mathrm{D}\left(\rho_f \boldsymbol{u}_p\right)}{\mathrm{D}t} - \frac{\mathrm{d}\left(\rho_f \boldsymbol{v}_p\right)}{\mathrm{d}t}\right], \tag{A1}$$

$$\frac{\mathrm{d}\boldsymbol{v}_p}{\mathrm{d}t} = \frac{\boldsymbol{u}_p - \boldsymbol{v}_p}{\tau_p} + \beta \frac{\mathrm{D}\boldsymbol{u}_p}{\mathrm{D}t} + \frac{\beta}{3\rho_f}\left[\boldsymbol{u}_p \frac{\mathrm{D}\rho_f}{\mathrm{D}t} - \boldsymbol{v}_p \frac{\mathrm{d}\rho_f}{\mathrm{d}t}\right]. \tag{A2}$$

From the mass conservation equation, we have

$$\frac{\mathrm{D}\rho_f}{\mathrm{D}t} = -\rho_f \boldsymbol{\nabla} \boldsymbol{\cdot} \boldsymbol{u}, \tag{A3}$$

$$\frac{\mathrm{d}\rho_f}{\mathrm{d}t} = \frac{\mathrm{D}\rho_f}{\mathrm{D}t} + \left(\boldsymbol{v}_p - \boldsymbol{u}_p\right) \boldsymbol{\cdot} \boldsymbol{\nabla}\rho_f. \tag{A4}$$

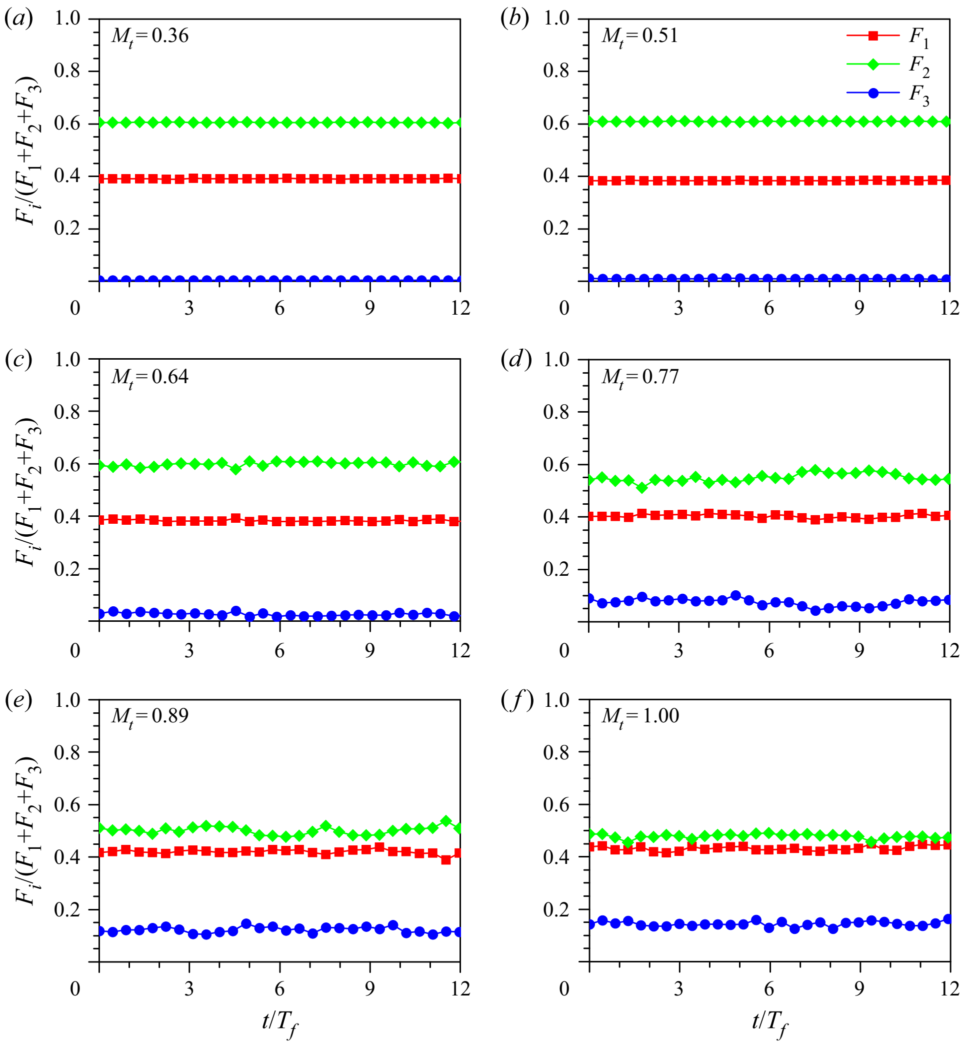

Figure 20. The average values of F_1, F_2 and F_3 among all particles at different time slices.

Substituting (A3) and (A4) into (A2), we get

$$\frac{\mathrm{d}\boldsymbol{v}_p}{\mathrm{d}t} = \frac{\boldsymbol{u}_p - \boldsymbol{v}_p}{\tau_p} + \beta\frac{\mathrm{D}\boldsymbol{u}_p}{\mathrm{D}t} + \left\{\frac{\beta}{3}\left(\boldsymbol{v}_p - \boldsymbol{u}_p\right)\boldsymbol{\nabla}\boldsymbol{\cdot}\boldsymbol{u}_p - \frac{\beta}{3\rho_f}\boldsymbol{v}_p\left[\left(\boldsymbol{v}_p - \boldsymbol{u}_p\right)\boldsymbol{\cdot}\boldsymbol{\nabla}\rho_f\right]\right\}. \tag{A5}$$

If St is small (τ_p is quite small), then $(\boldsymbol{v}_p - \boldsymbol{u}_p)$ in the third term on the right-hand side of (A5) will also be small as $\boldsymbol{v}_p = \boldsymbol{u}_p + O(\tau_p)$. However, in compressible flows, $\boldsymbol{\nabla}\boldsymbol{\cdot}\boldsymbol{u}_p$ and $\boldsymbol{\nabla}\rho_f$ will increase as M_t increases. Consequently, there is a question of whether the contribution of the third term on the right-hand side of (A5) can be neglected. Here, we define

$$\left.\begin{aligned} F_1 &= \left|\frac{\boldsymbol{u}_p - \boldsymbol{v}_p}{\tau_p}\right|, \\ F_2 &= \left|\beta \frac{\mathrm{D}\boldsymbol{u}_p}{\mathrm{D}t}\right|, \\ F_3 &= \left|\frac{\beta}{3}\left(\boldsymbol{v}_p - \boldsymbol{u}_p\right)\nabla\boldsymbol{\cdot}\boldsymbol{u}_p - \frac{\beta}{3\rho_f}\boldsymbol{v}_p\left[\left(\boldsymbol{v}_p - \boldsymbol{u}_p\right)\boldsymbol{\cdot}\nabla\rho_f\right]\right|, \end{aligned}\right\} \tag{A6}$$

and then measure the averages of F_1, F_2 and F_3 among all particles at different time slices, in order to have an *a priori* estimate of the importance of the neglected terms. In figure 20, we show that the contribution of F_3 is well below 5 % up to $M_t = 0.6$, and becomes of the order of 10–15 % only at the largest Mach number, $M_t = 1.00$. As a result, we argue that the approximation that we made is reasonably acceptable up to the largest Mach number that we have investigated, and we leave for future studies the question of checking the precise impact of the extra terms in (A5) for those Mach regimes.

References

Anderson, J.D. Jr 2010 *Fundamentals of Aerodynamics*. Tata McGraw-Hill Education.

Ayyalasomayajula, S., Gylfason, A., Collins, L.R., Bodenschatz, E. & Warhaft, Z. 2006 Lagrangian measurements of inertial particle accelerations in grid generated wind tunnel turbulence. *Phys. Rev. Lett.* **97** (14), 144507.

Ayyalasomayajula, S., Warhaft, Z. & Collins, L.R. 2008 Modeling inertial particle acceleration statistics in isotropic turbulence. *Phys. Fluids* **20** (9), 095104.

Barth, E.L. & Rafkin, S.C.R. 2007 TRAMS: a new dynamic cloud model for Titan's methane clouds. *Geophys. Res. Lett.* **34** (3), L03203.

Bec, J., Biferale, L., Boffetta, G., Celani, A., Cencini, M., Lanotte, A., Musacchio, S. & Toschi, F. 2006 Acceleration statistics of heavy particles in turbulence. *J. Fluid Mech.* **550**, 349–358.

Biferale, L., Boffetta, G., Celani, A., Devenish, B.J., Lanotte, A. & Toschi, F. 2004 Multifractal statistics of Lagrangian velocity and acceleration in turbulence. *Phys. Rev. Lett.* **93** (6), 064502.

Biferale, L. & Toschi, F. 2005 Joint statistics of acceleration and vorticity in fully developed turbulence. *J. Turbul.* **6**, N40.

Bourgoin, M. & Xu, H. 2014 Focus on dynamics of particles in turbulence. *New J. Phys.* **16** (8), 085010.

Bragg, A.D., Ireland, P.J. & Collins, L.R. 2015 Mechanisms for the clustering of inertial particles in the inertial range of isotropic turbulence. *Phys. Rev.* E **92** (2), 023029.

Coleman, S.W. & Vassilicos, J.C. 2009 A unified sweep-stick mechanism to explain particle clustering in two-and three-dimensional homogeneous, isotropic turbulence. *Phys. Fluids* **21** (11), 113301.

Curran, E.T., Heiser, W.H. & Pratt, D.T. 1996 Fluid phenomena in scramjet combustion systems. *Annu. Rev. Fluid Mech.* **28** (1), 323–360.

Dai, Q., Jin, T., Luo, K. & Fan, J. 2018 Direct numerical simulation of particle dispersion in a three-dimensional spatially developing compressible mixing layer. *Phys. Fluids* **30** (11), 113301.

Dai, Q., Luo, K., Jin, T. & Fan, J. 2017 Direct numerical simulation of turbulence modulation by particles in compressible isotropic turbulence. *J. Fluid Mech.* **832**, 438–482.

Federrath, C., Roman-Duval, J., Klessen, R.S., Schmidt, W. & Mac Low, M.-M. 2010 Comparing the statistics of interstellar turbulence in simulations and observations – solenoidal versus compressive turbulence forcing. *Astron. Astrophys.* **512**, A81.

Ferri, A. 1973 Mixing-controlled supersonic combustion. *Annu. Rev. Fluid Mech.* **5** (1), 301–338.

Fuster, D. & Colonius, T. 2011 Modelling bubble clusters in compressible liquids. *J. Fluid Mech.* **688**, 352–389.

Gatignol, R. 1983 The Faxén formulae for a rigid particle in an unsteady non-uniform Stokes flow. *J. Méc. Théor. Appl.* **1** (2), 143–160.

Goto, S. & Vassilicos, J.C. 2008 Sweep-stick mechanism of heavy particle clustering in fluid turbulence. *Phys. Rev. Lett.* **100** (5), 054503.

Gotoh, T. & Rogallo, R.S. 1999 Intermittency and scaling of pressure at small scales in forced isotropic turbulence. *J. Fluid Mech.* **396**, 257–285.

GUSTAVSSON, K. & MEHLIG, B. 2016 Statistical models for spatial patterns of heavy particles in turbulence. *Adv. Phys.* **65** (1), 1–57.

HAUGEN, N.E.L., BRANDENBURG, A., SANDIN, C. & MATTSSON, L. 2022 Spectral characterisation of inertial particle clustering in turbulence. *J. Fluid Mech.* **934**, A37.

HEISENBERG, W. 1985 Zur statistischen theorie der turbulenz. In *Original Scientific Papers Wissenschaftliche Originalarbeiten*, pp. 82–111. Springer.

HUETE, C., URZAY, J., SÁNCHEZ, A.L. & WILLIAMS, F.A. 2016 Weak-shock interactions with transonic laminar mixing layers of fuels for high-speed propulsion. *AIAA J.* **54** (3), 966–979.

JOHANSEN, A., OISHI, J.S., MAC LOW, M.-M., KLAHR, H., HENNING, T. & YOUDIN, A. 2007 Rapid planetesimal formation in turbulent circumstellar disks. *Nature* **448** (7157), 1022–1025.

KIDA, S. & ORSZAG, S.A. 1990 Energy and spectral dynamics in forced compressible turbulence. *J. Sci. Comput.* **5** (2), 85–125.

KOLMOGOROV, A.N. 1941*a* Dissipation of energy in the locally isotropic turbulence. *Dokl. Akad. Nauk SSSR* **31**, 538–540.

KOLMOGOROV, A.N. 1941*b* The local structure of turbulence in incompressible viscous fluid for very large Reynolds numbers. *Dokl. Akad. Nauk SSSR* **30**, 301–305.

LA PORTA, A., VOTH, G.A., CRAWFORD, A.M., ALEXANDER, J. & BODENSCHATZ, E. 2001 Fluid particle accelerations in fully developed turbulence. *Nature* **409** (6823), 1017–1019.

LAVEZZO, V., SOLDATI, A., GERASHCHENKO, S., WARHAFT, Z. & COLLINS, L.R. 2010 On the role of gravity and shear on inertial particle accelerations in near-wall turbulence. *J. Fluid Mech.* **658**, 229–246.

MAXEY, M.R. 1987 The gravitational settling of aerosol particles in homogeneous turbulence and random flow fields. *J. Fluid Mech.* **174**, 441–465.

MAXEY, M.R. & RILEY, J.J. 1983 Equation of motion for a small rigid sphere in a nonuniform flow. *Phys. Fluids* **26** (4), 883–889.

MONCHAUX, R., BOURGOIN, M. & CARTELLIER, A. 2012 Analyzing preferential concentration and clustering of inertial particles in turbulence. *Intl J. Multiphase Flow* **40**, 1–18.

MORDANT, N., CRAWFORD, A.M. & BODENSCHATZ, E. 2004 Three-dimensional structure of the Lagrangian acceleration in turbulent flows. *Phys. Rev. Lett.* **93** (21), 214501.

NI, R., HUANG, S.-D. & XIA, K.-Q. 2012 Lagrangian acceleration measurements in convective thermal turbulence. *J. Fluid Mech.* **692**, 395–419.

OTT, S. & MANN, J. 2000 An experimental investigation of the relative diffusion of particle pairs in three-dimensional turbulent flow. *J. Fluid Mech.* **422**, 207–223.

PAN, L., PADOAN, P., SCALO, J., KRITSUK, A.G. & NORMAN, M.L. 2011 Turbulent clustering of protoplanetary dust and planetesimal formation. *Astrophys. J.* **740** (1), 6.

PARMAR, M., HASELBACHER, A. & BALACHANDAR, S. 2011 Generalized Basset-Boussinesq-Oseen equation for unsteady forces on a sphere in a compressible flow. *Phys. Rev. Lett.* **106** (8), 084501.

PARMAR, M., HASELBACHER, A. & BALACHANDAR, S. 2012 Equation of motion for a sphere in non-uniform compressible flows. *J. Fluid Mech.* **699**, 352–375.

REISMAN, G.E., WANG, Y.-C. & BRENNEN, C.E. 1998 Observations of shock waves in cloud cavitation. *J. Fluid Mech.* **355**, 255–283.

STELZENMULLER, N., POLANCO, J.I., VIGNAL, L., VINKOVIC, I. & MORDANT, N. 2017 Lagrangian acceleration statistics in a turbulent channel flow. *Phys. Rev. Fluids* **2** (5), 054602.

TOSCHI, F. & BODENSCHATZ, E. 2009 Lagrangian properties of particles in turbulence. *Annu. Rev. Fluid Mech.* **41**, 375–404.

URZAY, J. 2018 Supersonic combustion in air-breathing propulsion systems for hypersonic flight. *Annu. Rev. Fluid Mech.* **50**, 593–627.

VEDULA, P. & YEUNG, P.-K. 1999 Similarity scaling of acceleration and pressure statistics in numerical simulations of isotropic turbulence. *Phys. Fluids* **11** (5), 1208–1220.

VOLK, R., CALZAVARINI, E., VERHILLE, G., LOHSE, D., MORDANT, N., PINTON, J.-F. & TOSCHI, F. 2008*a* Acceleration of heavy and light particles in turbulence: comparison between experiments and direct numerical simulations. *Physica* D **237** (14–17), 2084–2089.

VOLK, R., MORDANT, N., VERHILLE, G. & PINTON, J.-F. 2008*b* Laser Doppler measurement of inertial particle and bubble accelerations in turbulence. *Europhys. Lett.)* **81** (3), 34002.

VOTH, G.A., LA PORTA, A., CRAWFORD, A.M., ALEXANDER, J. & BODENSCHATZ, E. 2002 Measurement of particle accelerations in fully developed turbulence. *J. Fluid Mech.* **469**, 121–160.

VOTH, G.A., SATYANARAYAN, K. & BODENSCHATZ, E. 1998 Lagrangian acceleration measurements at large Reynolds numbers. *Phys. Fluids* **10** (9), 2268–2280.

WANG, J., WANG, L.-P., XIAO, Z., SHI, Y. & CHEN, S. 2010 A hybrid numerical simulation of isotropic compressible turbulence. *J. Comput. Phys.* **229** (13), 5257–5279.

Wang, L.-P., Wexler, A.S. & Zhou, Y. 1998 On the collision rate of small particles in isotropic turbulence. I. Zero-inertia case. *Phys. Fluids* **10** (1), 266–276.

Wang, X., Wan, M., Yang, Y., Wang, L.-P. & Chen, S. 2020 Reynolds number dependence of heavy particles clustering in homogeneous isotropic turbulence. *Phys. Rev. Fluids* **5**, 124603.

Wang, Y.C. & Brennen, C.E. 1999 Numerical computation of shock waves in a spherical cloud of cavitation bubbles. *Trans. ASME J. Fluids Engng* **121** (4), 872–880.

Wilkinson, M., Mehlig, B. & Bezuglyy, V. 2006 Caustic activation of rain showers. *Phys. Rev. Lett.* **97**, 048501.

Xiao, W., Jin, T., Luo, K., Dai, Q. & Fan, J. 2020 Eulerian–Lagrangian direct numerical simulation of preferential accumulation of inertial particles in a compressible turbulent boundary layer. *J. Fluid Mech.* **903**, A19.

Xu, H., Ouellette, N.T. & Bodenschatz, E. 2007*a* Curvature of Lagrangian trajectories in turbulence. *Phys. Rev. Lett.* **98** (5), 050201.

Xu, H., Ouellette, N.T., Vincenzi, D. & Bodenschatz, E. 2007*b* Acceleration correlations and pressure structure functions in high-Reynolds number turbulence. *Phys. Rev. Lett.* **99** (20), 204501.

Yaglom, A.M. 1949 On the acceleration field in a turbulent flow. *C. R. Akad. USSR* **67**, 795–798.

Yang, Y., Wang, J., Shi, Y., Xiao, Z., He, X.T. & Chen, S. 2013 Acceleration of passive tracers in compressible turbulent flow. *Phys. Rev. Lett.* **110** (6), 064503.

Yang, Y., Wang, J., Shi, Y., Xiao, Z., He, X.T. & Chen, S. 2014 Interactions between inertial particles and shocklets in compressible turbulent flow. *Phys. Fluids* **26** (9), 091702.

Yang, Y., Wang, J., Shi, Y., Xiao, Z., He, X.T. & Chen, S. 2016 Intermittency caused by compressibility: a Lagrangian study. *J. Fluid Mech.* **786**, R6.

Yeung, P.K. 1997 One- and two-particle Lagrangian acceleration correlations in numerically simulated homogeneous turbulence. *Phys. Fluids* **9** (10), 2981–2990.

Yeung, P.-K. & Pope, S.B. 1989 Lagrangian statistics from direct numerical simulations of isotropic turbulence. *J. Fluid Mech.* **207**, 531–586.

Zhang, Q., Liu, H., Ma, Z. & Xiao, Z. 2016 Preferential concentration of heavy particles in compressible isotropic turbulence. *Phys. Fluids* **28** (5), 055104.

Zhang, Q. & Xiao, Z. 2018 Single-particle dispersion in compressible turbulence. *Phys. Fluids* **30** (4), 040904.

Zhang, Z., Legendre, D. & Zamansky, R. 2019 Model for the dynamics of micro-bubbles in high-Reynolds-number flows. *J. Fluid Mech.* **879**, 554–578.

Zhou, Y., Wexler, A.S. & Wang, L.-P. 1998 On the collision rate of small particles in isotropic turbulence. II. Finite inertia case. *Phys. Fluids* **10** (5), 1206–1216.